Load- and Position-Independent Moving MHz WPT System Based on GaN-Distributed Current Sources

Alex Pacini, *Graduate Student Member, IEEE*, Alessandra Costanzo, *Senior Member, IEEE*, Samer Aldhaher, and Paul D. Mitcheson, *Senior Member, IEEE*

***Abstract*— This paper describes the modeling, analysis, and design of a complete (dc-to-dc) inductive wireless power transfer (WPT) system for industrial moving applications. The system operates at 6.78 MHz and delivers up to 150 W to a load moving along a linear path, providing a quasi-constant dc output voltage and maintaining a zero voltage switching operation, regardless of position and load, without any retuning or feedback. The inductive link consists of an array of stationary transmitting coils and a moving receiving coil whose length is optimized to achieve a constant coupling coefficient along the path. Each Tx coil is individually driven by a constant amplitude and phase sinusoidal current that is generated from a GaN-based coupled load-independent Class EF inverter. Two adjacent transmitters are activated at a given time depending on the receiver's position; this effectively creates a *virtual* series connection between the two transmitting coils. The Rx coil is connected to a passive Class E rectifier that is designed to maintain a constant dc output voltage independent of its load and position. Extensive experimental results are presented to show the performance over different loading conditions and positions. A peak dc-to-dc efficiency of 80% is achieved at 100 W of dc output power and a dc output voltage variation of less than 5% is measured over a load range from 30 to 500 Ω. The work in this paper is foreseen as a design solution for a high-efficient, maintenance-free, and reliable WPT system for powering sliders and mass movers in industrial automation plants.**

***Index Terms*— Autonomous vehicles, inductive power transmission, intelligent vehicles, resonant inverters, wide bandgap semiconductors, wireless power transmission.**

I. Introduction

INDUSTRIAL automation plants rely on machinery and tools for a wide range of processes and applications. Delivering power using cables to moving machines and tools can constrain their freedom of operation. In addition, a common failure mechanism in many applications is due to cable degradation and loose connectors, which occurs due to wear and tear from the repeated mechanical stress and pressure. Inductive wireless power transfer (WPT) can enhance reliability and functionality [1]–[7], since the need of cables and connectors is reduced. WPT can also enable real-time machine testing, by combing wireless data and power transfer [8].

A key feature of a dynamic WPT system is the ability to deliver consistent performance over different loads and position while maintaining high efficiency and constant output voltage. Current solutions in the literature show excellent efficiencies but only for static scenarios and at fixed loads as they are strongly dependent on the receiver's position. In [9], a wide range of operating frequencies for resonance tracking is required. To overcome the problem of variable couplings, a long single transmitting coil is adopted in [10], but it suffers from low efficiency due to the huge leakage inductance, which decreases its kQ product [11]. A segmented system composed of multiple active Tx coils is proposed in [12] and [13], but the powering and receiving subsystems are not detailed. Reference [14] proposes six Tx coils always powered and connected in parallel. However, parallel-connected Tx coils have been demonstrated to be a suboptimal solution, if the

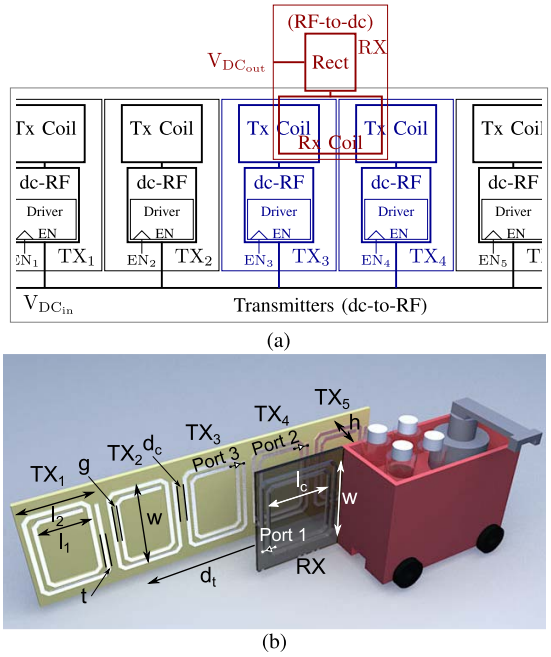

Fig. 1. Moving WPT link powered by a linear array of planar Tx modules: a segment of five is shown, but the system can be extended to cover any linear path. Only two Txs are active at each time (blue box), depending on the Rx (red box) position. (a) Block diagram and (b) rendered illustration of an industrial slider. For the present design at 6.78 MHz, the dimensions in cm are: $l_c = 17.2$, $l_1 = 12$, $l_2 = 18$, $d_c = 2$, $w = 24$, $g = 1$, $t = 1$, and $h = 6$.

Manuscript received July 1, 2017; revised September 27, 2017; accepted October 20, 2017. Date of publication December 4, 2017; date of current version December 12, 2017. This paper is an expanded version from the 2017 IEEE MTT-S International Microwave Symposium Conference, Honolulu, HI, USA, on June 4–9, 2017. *(Corresponding author: Alex Pacini.)*

A. Pacini is with the Department of Electrical, Electronic and Information Engineering "G. Marconi," University of Bologna, 47521 Bologna, Italy (e-mail: alex.pacini@studio.unibo.it).

A. Costanzo is with the Department of Electrical, Electronic and Information Engineering "G. Marconi," University of Bologna, 47521 Bologna, Italy, and also with ARCES (e-mail: alessandra.costanzo@unibo.it).

S. Aldhaher and P. D. Mitcheson are with the Control and Power Group, Imperial College London, London SW7 2AZ, U.K. (e-mail: paul.mitcheson@imperial.ac.uk).

Color versions of one or more of the figures in this paper are available online at http://ieeexplore.ieee.org.

Digital Object Identifier 10.1109/TMTT.2017.2768031

Tx-to-Rx distance is variable [15], [16]. Multiple active transmitters are also proposed in [17], but again this approach is still limited to the description of the RF link alone. Furthermore, a long feeding line is needed for powering, hence increasing the parasitic inductances. A way to solve misalignment issues in a limited path is introduced in [18], but a parallel connection of the Tx coils is still adopted.

This paper expands upon [19], where the model of a novel modular moving WPT system is proposed. It consists of distributed RF power sources driving an array of stationary transmitting Tx coils, with one pair of Tx coils virtually series-connected and active at a time, depending on the sliding Rx module position. This paper provides the entire dc-to-dc system design and characterization together with its experimental evaluation. New design solutions are adopted to comply with the actual behavior of each subsystem block. The full experimental characterization of the Class EF inverter in coupled configuration is discussed and the experimental results are provided. Important aspects of the real system implemetation are highlighted, that were not evident from the theoretical and numerical analysis presented in [19]. The critical impact of the coupled inverters output current phase imbalance is discussed in detail and confirmed by measurements. On the mobile receiver side, the rectifier is redesigned as a Class E topology instead of a Class EF, which also maintains zero reactance and constant voltage, as required by the coupled inverters but with a higher efficiency and a larger C_1 value.

The design starts by optimizing the inductive link to achieve a position-independent coupling coefficient. This is done by selecting the optimum Rx coil geometry with respect to the Tx coil as shown in [15]. A pair of Tx coils are series connected, *virtually*, by means of identical coupled load-independent Class EF inverters. GaN HEMTs are used to achieve improved efficiencies and higher power densities, with the system switching at 6.78 MHz. A Class E rectifier is then designed by means of the nonlinear harmonic balance (HB) technique to ensure a quasi-resistive input impedance and a constant dc output voltage for all the Rx positions and dc loads of interest. In this way, a fully modular and periodic WPT system, whose length can be arbitrarily extended depending on the specific need, is demonstrated to be possible. A further added value of the proposed architecture is that only a dc feeding line and the control logic signals are needed along the powering path. In this way, any undesired reactive parasitic effects and RF losses along the path are absent and high WPT operating frequencies are enabled. A representative slice of the modular moving WPT system, consisting of four complete Tx modules and one Rx receiver sliding over them, is prototyped and an extensive experimental characterization is presented to validate the design procedure.

For the demonstrative part of the system design, the activation/deactivation of the switches is performed manually. These operations can be straightforwardly implemented by a suitable control logic unit driven by the sensing of the Rx position. The inverters are easily synchronized by driving them with the same gate signal. Since the switching mechanisms are already fully accounted for, the system efficiency is not expected to be influenced.

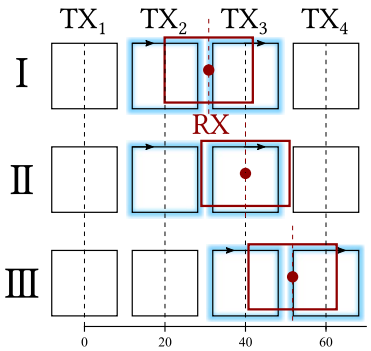

Fig. 2. Pair of series-connected Tx coils (blue box) with respect to the Rx positions (cm) (red box). I and III correspond to all the Rx coil positions located between two subsequent Tx coils. II shows the Rx position where Tx coils switching is needed: TX_2 is deactivated and TX_4 activated. The sequence is repeated all over the transmitting path.

Given the high operating frequency of 6.78 MHz, the moving WPT system is tested in a quasi-static regime approximation, that is, by means of snapshots of the receiver positions. Indeed, the switching period is orders of magnitude shorter than the Rx time-of-flight between two Txs.

II. Codesign of the Entire Moving WPT Link

This section describes the theoretical and numerical approaches for the piecewise design of a modular moving inductive WPT system. The goal is to achieve a position-independent coupling coefficient resulting in a constant dc output voltage regardless of load and position. Fig. 1(a) shows a block diagram of the system, which consists of three main blocks (or subsystems): 1) the still inverters (dc-to-RF); 2) the inductive WPT link (RF-to-RF); and 3) the moving rectifier (RF-to-dc).

A. Electromagnetic Design of the RF-to-RF Link

To solve the issue of variable couplings in a dynamic WPT system, an array of coils is used at the Tx side [15], [16]. This choice allows a more efficient powering of the sliding path compared with long single transmitting coil. By connecting in series two transmitting coils at a time and by optimizing the Rx coil layout, a position-independent coupling coefficient is obtained. In [15], it has been analytically and experimentally demonstrated that the flat coupling coefficient behavior is retained also for various Rx vertical distances.

The system illustration of Fig. 1(b) shows the fixed array of planar Tx coils, at a prescribed distance from each other, facing the moving Rx. The geometrical dimensions, optimized for 6.78 MHz, are reported in caption of Fig. 1. They are obtained by optimizing a set of three-port networks composed of two active Tx coils and a moving Rx one for constant coupling coefficient. Each three-port network represents the system with a different l_c value and a different Rx position. Twenty different receiver positions and the associated three-port networks are considered, with the receiver axis moving from 20 to 30 cm (see Fig. 2). The space-periodic path is schematically represented in Fig. 2, where the active coils are outlined depending on the Rx positions. In case I, only TX_2 and TX_3 are powered. The Rx movement from 30 to 40 cm can be derived by mirroring the previous one, due to the symmetry.

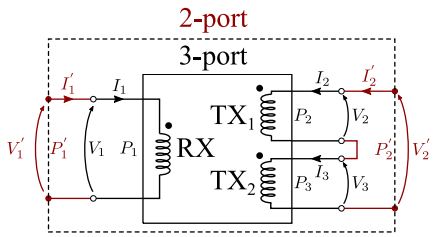

Fig. 3. Equivalent circuit of the instantaneous RF link: the three-port network, representing two independent active Tx coils coupled with the Rx one, reduces to a two-port network when the Tx coils are series-connected.

When the receiver axis aligns with the TX_3 axis, case (II), TX_2 must be turned OFF and TX_4 must be activated, allowing to periodically reproduce the same behavior from 20 to 40 cm. Therefore, the spatial periodicity of the system enables a theoretically unlimited path. By connecting in series the two active Tx coils (see Fig. 3), the interaction between the magnetic fields allows the resulting shared flux at the receiver coil to be constant.

The initial Rx coil length, l_c^{opt}, is computed geometrically in ideal conditions by means of the following relationship:

$$l_c^{\text{opt}} = l_1 + \frac{l_2 - l_1}{2} + d_c \tag{1}$$

which is valid if the coils are assumed to be solenoids having the same current, hence a uniform magnetic field inside them and zero outside. Ideal conductors are assumed and all the parasitic effects are neglected. By segmenting the coil turns into elementary areas, the overall shared magnetic flux can be calculated by means of superposition of the elementary contributions. The optimum value of $l_c = l_c^{\text{opt}}$ is derived by assuming that when the receiver slides to the right, the flux lost at its left-hand side is exactly reintroduced at the right-hand side. Afterward, realistic coils are used in a full-wave EM simulation [20] of the RF link layout, to derive the $\boldsymbol{Z}$ matrix of the three-port network in Fig. 3. By recalling the generic coupling coefficient of two coils, L_a and L_b, with mutual inductance M_{ab}

$$k_{ab} = \frac{M_{ab}}{\sqrt{L_a L_b}}. \tag{2}$$

The imaginary parts of $\boldsymbol{Z}$, $X_{ij} = \text{Im}\{Z_{ij}\}$ are used to compute the three coupling coefficients characterizing the RF link (see Fig. 3), one between the two Txs, k_{TX}, and two between each Tx and Rx, k_{RX_1} and k_{RX_2}

$$k_{\text{RX}_1} = \frac{X_{12}}{\sqrt{X_{11}X_{22}}} \quad k_{\text{RX}_2} = \frac{X_{13}}{\sqrt{X_{11}X_{22}}} \quad k_{\text{TX}} = \frac{X_{23}}{X_{22}} \tag{3}$$

with $X_{22} = X_{33}$, since the transmitters are assumed identical. After the series connection of the two Tx coils ($I_2 = I_3 = I_2'$, $V_2 + V_3 = V_2'$, and $I_1 = I_1'$), the resulting *virtual* two-port network relationships are obtained

$$\begin{aligned} V_1' &= Z_{11}I_1' + (Z_{12} + Z_{13})I_2' \\ V_2' &= (Z_{12} + Z_{13})I_1' + (Z_{22} + Z_{23} + Z_{23} + Z_{22})I_2' \end{aligned} \tag{4}$$

where reciprocity holds. Simplifying 4, the coupling coefficient of the RF link after the two Tx series connection is derived

$$k_{\text{RX}_S} = \frac{1}{\sqrt{2}} \frac{k_{\text{RX}_1} + k_{\text{RX}_2}}{\sqrt{1 + k_{\text{TX}}}}. \tag{5}$$

The predicted impact of l_c on the link coupling coefficient, as the Rx is moving, is plotted in Fig. 4 with the normalized length l_c/l_1 as a parameter. Normalized plots allow an agile scaling of the whole system without affecting the performance as long as the parasitic effects are negligible. From Fig. 4, it is clear that $l_c/l_1 = 1.43$, which corresponds to $l_c = 17.2$ cm, ensures a constant coupling all over the sliding path, thus confirming the validity of the approximated approach introduced by (1). The corresponding measurements are superimposed in Fig. 5: an excellent flatness of k_{RX_S} is observed for the selected l_c. Details of the setup are discussed in Section III. Finally, k_{RX_S} with l_c^{opt} is computed for different Rx–Tx distances h and the associated plots are shown in Fig. 5, confirming that l_c^{opt} ensures position-independent performances. The measured data, for $h = 6$ and 10 cm, are superimposed in the same

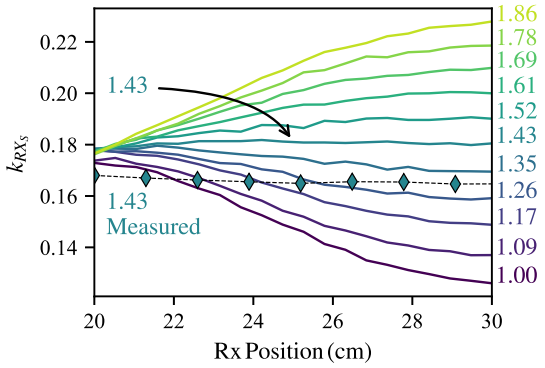

Fig. 4. Coupling coefficients of the *virtual* two-port for different normalized Rx coil l_c/l_1 versus variable Rx displacements: 20 cm corresponds to the Rx axis aligned with the TX_2 axis and 30 cm to Rx axis located in the middle of the TX_2 and TX_3 axes. The displacement is given in centimeters to avoid confusion in the following, but can be normalized to l_1 as well. Only for $l_c/l_1 = 1.43$, k_{RX_S} does not vary all over the Rx path. The diamonds are the corresponding measured data. The Rx plane distance from the Tx plane is $h/l_1 = 0.5$ (h =6 cm; see Fig. 1).

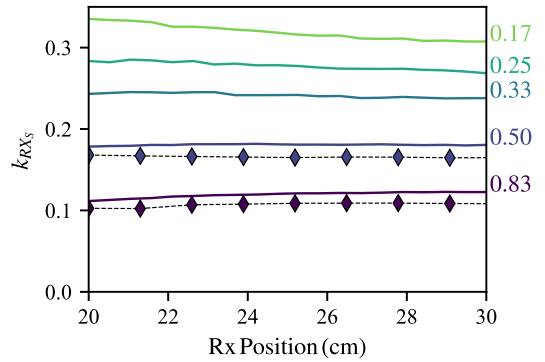

Fig. 5. Coupling coefficient of the *virtual* two-port with $l_c/l_1 = 1.43$ for different distances h/l_1. The displacement is given in cm to avoid confusion in the following, but can be normalized to l_1 as well. The series connected link maintains its position-independent coupling coefficient at any Rx height (see Fig. 1). Diamonds are the measured data.

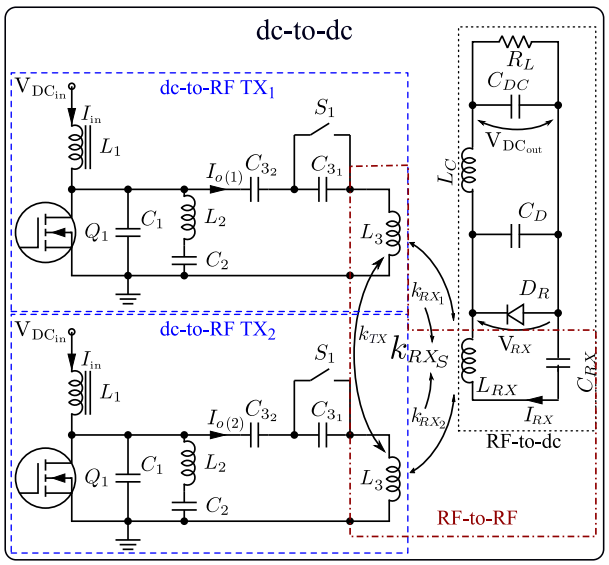

Fig. 6. *Instantaneous* dc-to-dc moving WPT system. On the Tx side, the dc-to-RF subsystem consists of two identical current sources exciting two coupled Tx coils L_3. To form the RF-to-RF subsystem, they are coupled to the Rx coil, L_{RX}. On the Rx side, the RF-to-dc subsystem is a class E rectifier terminated on a resistive load (variable).

Fig. 5: slightly lower values of k_{RX_S} have been experimentally obtained, but the flatness is confirmed for any Rx height. $h = 6$ cm is selected for the prototype.

It should be noted that the demonstrated constant coupling coefficient is obtained by the concurrence of the layout optimization that ensures the spatial periodicity and the series connection of two transmitters that are satisfied by a moving system along a linear path. On the contrary, a rotation or a lateral displacement that deviate the system from such periodicity can cause a degradation of the coupling coefficient.

B. Coupled Class EF Inverters for Constant RF Current

To ensure the series connection of the active couple of Tx coils while keeping the full modularity of the transmitting system, a coupled load-independent Class EF inverter, similar to the one proposed in [21], is adopted as the power source of each Tx coil. This topology is reported in Fig. 6, where two identical inverters driving two coupled inductors are shown: each inverter consists of a single GaN HEMT (Q_1), with a parallel reactive network designed to ensure zero voltage switching (ZVS) operation. In the first step, the Rx is not yet considered, or, equivalently, $k_{RX_S} = 0$.

The ZVS is accomplished by the parallel connection of the output capacitance C_1 with the series branch $C_2 - L_2$, which is optimized to resonate at a frequency between the inverter switching frequency, 6.78 MHz, and its second harmonic. When S_1 is open, C_{3_1} and C_{3_2} are connected in series with the Tx coil L_3, to provide the proper residual inductance. This topology maintains the ZVS operation, while achieving a constant output current, for a wide range of loads without any need of retuning or components replacement. The useful feature of this inverter, to be exploited in the present distributed WPT system, is to provide a constant load-independent RF output current, enabling the *virtual* series connection of the two Tx coils.

First, following the numerical procedure presented in [21], the circuit parameters for the stand alone inverter are obtained: $L_1 = 88$ μH (RF Choke), $L_2 = 270$ nH, $L_3 = 1.42$ μH, $C_1 = 830$ pF (which includes the capacitance of Q_1), $C_2 = 718$ pF, $C_3 = 480$ pF, and duty cycle $D = 0.32$. In such conditions, the proper inverter resistive load can vary between 0 and 6 Ω.

When two nearby Tx coils are powered, the coupling between them, k_{TX} in Fig. 6, significantly modifies the load impedance of each inverter and the stand-alone topology can be used only as a starting point for the design of the two coupled inverters. Assuming the same L_3 value for the two inverters, the coupled inverter design can start from the voltages and currents relationships at Tx coil ports

$$\begin{aligned} V_{L_3(1)} &= (R_{L_3} + j\omega L_3) I_{o(1)} + j\omega M_{TX} I_{o(2)} \\ V_{L_3(2)} &= j\omega M_{TX} I_{o(1)} + (R_{L_3} + j\omega L_3) I_{o(2)} \end{aligned} \tag{6}$$

where L_3 and R_{L_3} are the coils inductance and loss resistance, respectively, and $M_{TX} = k_{TX} L_3$. The currents $I_{o(2)}$ and $I_{o(1)}$ that ideally should be the same, if the assumption of *virtual* series connection holds, can be expressed as

$$I_{o(1)} = A e^{-\frac{j\phi}{2}} I_o, \;\; I_{o(2)} = B e^{\frac{j\phi}{2}} I_o \tag{7}$$

where $A, B \in \mathbb{R}^+$, $\phi \in \mathbb{R}$ and $I_o \in \mathbb{C}$. Using (6), each Tx coil impedance, $Z_{L_3(n)}$ with $n \in \{1, 2\}$, in the absence of a receiver, can be computed as

$$Z_{L_3(n)} = \frac{V_{L_3(n)}}{I_{o(n)}} = R_{L_3} + j\omega L_3 + j\omega M_{TX} \alpha_n \tag{8}$$

where $(\alpha_n) = (\alpha_1, \alpha_2) = (B/Ae^{j\phi}, A/Be^{-j\phi})$.

The actual inductances at each inverter output, $L_{TX(n)}$, taking into account the coupling are

$$L_{TX(n)} = \frac{\mathrm{Im}\{Z_{L_3(n)}\}}{\omega} = L_3 + |\alpha_n| M_{TX} \cos(\phi). \tag{9}$$

Thus, accounting for the Tx coils coupling is mandatory, because the effective inductances, loading each coupled inverter, are different from those at the output of a stand-alone inverter.

Furthermore, differences in the current phases (ϕ) of each coupled Tx coil result in power transferred between the inverters ($P_{t(n)}$) that can be evaluated using the real part of (8)

$$\mathrm{Re}\{Z_{L_3(n)}\} = R_{L_3} + \omega M_{TX} |\alpha_n| \sin(\phi_n) \tag{10}$$

$$P_{t(n)} = \omega M_{TX} |\alpha_n| \sin(\phi_n) \left| I_{o(n)} \right|^2 \tag{11}$$

where $(\phi_n) = (\arg\{\alpha_1\}, \arg\{\alpha_2\}) = (\phi, -\phi)$.

Since $P_{t(1)} = -P_{t(2)}$, the linear network alone does not introduce losses, but if the inverter is included, a phase difference can compromise its ZVS operation due to an additional voltage component induced from the current through the coupled coil that is not synchronized with the inverter operation. Indeed, the switching clocks of both inverters are synchronized (or supplied from a common source) by the design, and an unwanted induced voltage is inevitably affecting the ZVS. The closed switch shorts this induced voltage, causing high

currents and losses. Moreover, a variation of the residual inductance, as in (9), even if negligible for small phase impairments, affects the ZVS due to detuning, since the inverter is not tolerant to variations of its reactance termination. On the contrary, a current magnitude variation, $|\alpha_n|$, produces similar effects on the ZVS but only due to the residual inductance, because, without any phase impairment, the power transferred between the Tx coils is always zero [$\sin(\phi_n) = 0$]. Besides an efficiency degradation, this also means that Q_1 can experience overheating.

The quality factor of the virtual inductor $L_{\mathrm{TX(n)}}$ is

$$Q_{L_{\mathrm{TX}}(n)} = \frac{\omega(L_3 + |\alpha_n| M_{\mathrm{TX}} \cos(\phi))}{R_{L_3} + \omega M_{\mathrm{TX}} |\alpha_n| \sin(\phi_n)} \tag{12}$$

or equivalently, using the relation $M_{\mathrm{TX}} = k_{\mathrm{TX}} L_3$

$$Q_{L_{\mathrm{TX}}(n)} = \frac{1 + |\alpha_n| k_{\mathrm{TX}} \cos(\phi)}{Q_{L_3}^{-1} + |\alpha_n| k_{\mathrm{TX}} \sin(\phi_n)} \tag{13}$$

where $Q_{L_3} = (\omega L_3)/R_{L_3}$ is the quality factor of L_3.

Since a key feature is to achieve currents with equal amplitudes, it is possible to approximate $|\alpha_n| \simeq 1$. Therefore,

$$L_{TX(n)} \simeq L_3 + M_{\mathrm{TX}} \cos(\phi) \simeq L_3 + M_{\mathrm{TX}} \tag{14}$$

where $\cos(\phi) \simeq 1$ for small angles ϕ. Equivalently,

$$L_{TX(n)} \simeq L_3(1 + k_{\mathrm{TX}}). \tag{15}$$

The resistive part becomes

$$\mathrm{Re}\{Z_{L_3(n)}\} \simeq R_{L_3} + \omega M_{\mathrm{TX}} \phi_n \tag{16}$$

with $\sin(\phi_n) \simeq \phi_n$ for small angles ϕ_n.

For this setup, the Tx coils are modeled as $k_{\mathrm{TX}} = -0.0595$, $L_3 = 1.42\ \mu$H, $R_{L_3} = 0.15\ \Omega$, and $\omega = 2\pi 6.78\mathrm{e}6$ rad/s. Since the coupling k_{TX} is negative, $L_{\mathrm{TX(n)}} = 1.34\ \mu$H, smaller than L_3.

The next step is to guarantee the proper residual inductance [22] to each coupled inverter. Let $L_{3,r}$ be the desired one for the stand-alone inverter, which is the result of the $C_3 - L_3$ series. When the *virtual* $L_{TX(n)}$ loads the inverter in place of L_3, the proper compensating capacitor $C'_{3(n)}$, which provides $L_{3,r}$, is computed as

$$L_{3,r} = L_3 - \frac{1}{C_3 \omega^2} \qquad L_{TX,r(n)} = L_{\mathrm{TX}} - \frac{1}{C'_{3(n)} \omega^2}. \tag{17}$$

Forcing $L_{3,r} = L_{TX,r(n)}$ and using (15)

$$C'_{3(n)} = \frac{C_3}{1 + (\frac{\omega}{\omega_r})^2 k_{\mathrm{TX}}}, \quad \text{where} \quad \omega_r = \frac{1}{\sqrt{C_3 L_3}} \tag{18}$$

where C_3 is the optimal value for the stand-alone inverter [21] and $C'_{3(n)}$ is the corresponding one for the coupled case.

The last issue to be discussed is to limit the currents induced in the nonactive Tx coils due to the currents flowing in the activated coils. From circuit simulation, it is shown that without any countermeasure, these currents are of the same order of magnitude of the desired ones, resulting in additional losses and detuning of the active inverters. To minimize this paper, the capacitor $C'_{3(n)}$ is split into two C_{3_2} and C_{3_1}, with $C_{3_2} > C_{3_1}$, and a switch (S_1 in Fig. 6) is connected in parallel to the smaller capacitor: if the inverter is OFF, the switch is closed; if the inverter is ON, the switch is open. In this way, if the inverter is OFF, its load is strongly detuned and the resulting output current is minimized. Furthermore, this solution avoids to short the $V_{\mathrm{dc_{in}}}$ supply, which would happen by shorting a single $C'_{3(n)}$. To determine C_{3_1} and C_{3_2} values, their series connection is chosen to be equal to $C'_{3(n)}$. Let $C_{3_2} = \beta C_{3_1}$, it follows that:

$$C_{3_1} = C'_{3(n)}(\frac{\beta + 1}{\beta}) \qquad C_{3_2} = C'_{3(n)}(\beta + 1). \tag{19}$$

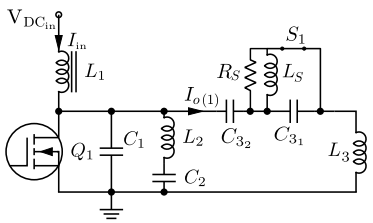

Fig. 7. Modified Class EF inverter in the OFF state: S_1 is closed, the inverter is detuned, and the current $I_{o(1)}$ is negligible.

A snubber, formed by R_S and L_S, is also connected in series to S_1 to mitigate the current peaks through the charged C_{3_1} when the switch is closed.

The designed values of these components are: $C_{3_1} = 530$ pF, $C_{3_2} = 4.70$ nF (hence $C'_{3(n)} = 480$ pF and $\beta \sim 9$), $R_S = 10\ k\Omega$, and $L_S = 250$ nH. An inactive Tx module is shown in Fig. 7.

Fig. 6 shows the circuit schematic of the end-to-end (dc-to-dc) link with two active Tx modules and the Rx coil loaded by a Class E rectifier similar to the one designed and experimentally verified in [23] and [24]. The modified design Class E rectifier is detailed in Section II-C.

In the next step, to evaluate the dc-to-RF subsystem in different positions, the receiver is introduced as a series resonant RLC load (with $k_{\mathrm{RX_S}} \neq 0$), which allows to check if the coupled inverters sustain the same current through the Tx coils. It also allows verifying that the output voltage on the resistive load is independent of both the Rx position and the load. The values of the components at the Rx side are: $L_{\mathrm{RX}} = 1.7\ \mu$H and $C_{\mathrm{RX}} = 324$pF. $k_{\mathrm{RX_1}}$ and $k_{\mathrm{RX_2}}$ are derived by full-wave EM simulation of the coupled-coil three-port RF link. From the measurements, the coupling coefficients resulted to be 10% lower than predicted (see Fig. 4), which in turn results in an effective $k_{\mathrm{RX_S}}$ of about 0.16.

First, the circuit of Fig. 6 is simulated in time domain, with the rectifier replaced by a variable resistive load, for several receiver positions and loads: for each of the 20 Rx positions previously considered. The performance with respect to 30 different loads are evaluated, from 10 Ω to 1 kΩ. Fig. 8(a) shows the currents through each Tx coil, whereas Fig. 8(b) shows the voltage across the resistive Rx load. The input dc voltage ($V_{\mathrm{dc_{in}}}$) is 70 V. All these plots are practically superimposed, proving that the coupled inverters are able to work as load-independent current sources, with the *virtual* series connection between the two Tx active coils confirmed.

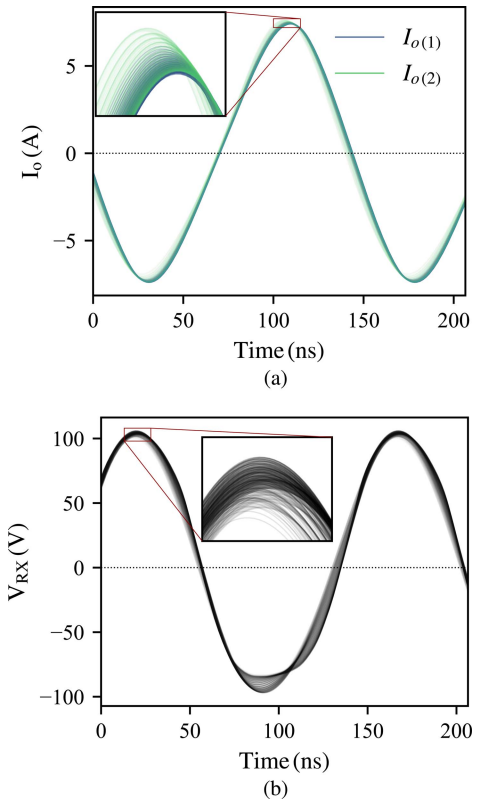

Fig. 8. (a) Load and position-independent waveforms of the currents exciting the two coupled Tx coils. (b) Voltages on the load (purely resistive and which replaces the rectifier in Section II-B) for $V_{dc_{in}}$ of 70 V. Results are from a set of 600 nonlinear/EM cosimulations spanning a 10-cm Rx displacement (20 different Rx positions) and 30 loads from 10 Ω to 1 kΩ. The curves are almost indistinguishable; insets highlight the differences.

C. Rectifier and Complete DC-to-DC Link

To ensure the same performances discussed previously, the rectifier is required to present a constant output voltage and a purely resistive input impedance, over the range of RF input power of interest, for any possible Rx position and loading conditions. This is a challenging task and, to the best of our knowledge, it is still unresolved. Indeed, the design of a standard Class E rectifier [22], [23] cannot be adopted for the present case, because its input reactance is dependent on the duty-cycle, which is a function of the dc load. Furthermore, in a moving system, such reactance varies with the Rx position and, once reflected to the Tx side, would degrade its performances, which are based on the (resistive-)load-independent coupled inverters. For a given excitation, the nonlinear reflected impedance $Z'_{RX(n)}$, which effectively loads the inverter, can be written as

$$Z'_{RX(n)} = \frac{\omega^2 M^2_{RX(n)}}{Z_{RX}} \tag{20}$$

where $M_{RX(n)} = k_{RX(n)}\sqrt{L_3 L_{RX}}$ is the mutual inductance between an active Tx coil and the Rx one, and Z_{RX} is the rectifier input impedance (V_{RX}/I_{RX}) at the fundamental harmonic. Since $M_{RX(n)}$ strongly depends on the Rx position, a constant imaginary part of Z_{RX} still produces a significant variation of $Z'_{RX(n)}$ while the Rx is moving. Thus, the rectifier has to provide a quasi-zero imaginary part of $Z'_{RX(n)}$ for any dc-load of interest.

The Class-E resonant rectifier [25] with a quasi-resistive-input is used as a starting point. Although this solution is able to reduce the reactive part of Z_{RX}, by a proper choice of C_D and by allowing for a ripple of the output current by reducing L_C, it results in a output voltage strongly dependent on the dc load, which is not an acceptable solution for the system under consideration. For this reason, an HB-based optimization of the whole dc-to-dc system is carried out, spanning all the possible Rx loads and positions. The RF choke, L_C, is reintroduced. The capacitors C_{RX} and C_D (Fig. 6) are included among the design variables. Two main goals are pursued: the maximization of the dc-to-dc efficiency and the minimization of the dc output voltage variations, which imply minimizing the imaginary part of $Z'_{RX(n)}$. A total number of system configurations equal to 600 is considered, covering 20 Rx positions and 30 loads. The nonlinear regime is described using 16 harmonics. $V_{dc_{in}}$ is 70 V, which is the best tradeoff between maximum output dc power, efficiency, and safety for the experimental verification. The losses are accounted for by resistances in series with the respective inductances and are computed as: $R_{L_1} = 2\ \Omega$, $R_{L_2} = 0.06\ \Omega$, $R_{L_3} = 0.15\ \Omega$, $R_{L_{RX}} = 0.2\ \Omega$, and $R_{L_C} = 2\ \Omega$. Q_1 is modeled as a switch with a series resistance of 50 mΩ while the remaining components are ideal. The other circuit elements are: $L_{RX} = 1.7\ \mu$H, $L_C = 88\ \mu$H, and $C_{dc} = 20\ \mu$F. The diode is the Schottky SiC Wolfspeed/CREE C3D1P7060Q, chosen to sustain high current/voltage capability and has a low capacitance. To comply with high current peaks, two diodes are connected in parallel thanks to the positive temperature coefficient of SiC diodes, which results in equal sharing of currents, and are included in the simulation using their SPICE model. The optimized capacitors are: $C_{RX} = 498$ pF and $C_D = 33$ pF.

The predicted dc output power is 100 W on a 38-Ω load with a dc–dc efficiency of 80% calculated as

$$\eta = \frac{P_{dc_{out}}}{P_{dc_{in}}}. \tag{21}$$

The voltage variation is under 5%, for any load value over 30 Ω. After the nonlinear optimization, the imaginary part of the impedance $Z'_{RX(n)}$, monitored for all the system configurations discussed previously (Rx positions and loads) is always lower than $0.2j$, corresponding to an L_3 variation under 5 nH, or 0.3%. This ensures the proper switching operation (ZVS) of the inverters.

III. Experimental Setup and Measurements

The measurement setup is composed of four identical Tx modules (one is shown in Fig. 9) and is reported in Fig. 10. Details of the inverter and the rectifier are shown in Figs. 11 and 12, respectively. Q_1 is a GaN System GS66504B Enhancement HEMT GaN FET. The powering path, as extended as necessary, is obtained by placing side-by-side other transmitter modules, like "Lego" tiles. Therefore, the system only requires a single dc-feed line along the whole path while the RF signal is generated on board at the active

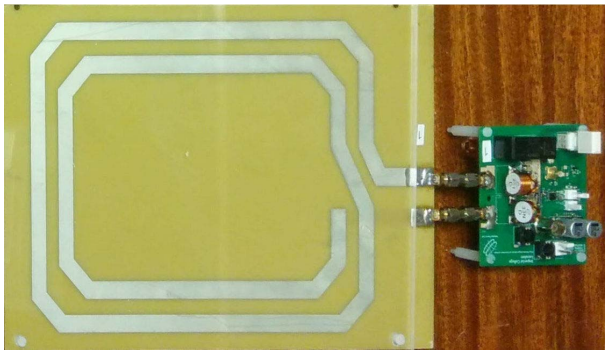

Fig. 9. Photograph of a single TX module.

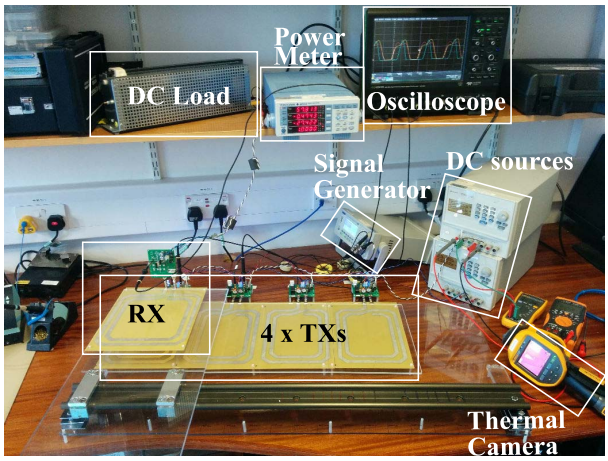

Fig. 10. DC-to-dc link setup: four Tx coils, each one driven by its own inverter, with an Rx subsystem sliding over them at a vertical separation of 6 cm. The GaN FET is driven by an ISL5511IRZ high-speed MOSFET IC driver with a gate voltage of 5 V. The variable load is connected to the dc output and spans from 30 to 120 Ω (higher resistances are obtained by a series connection of 100-Ω power resistors). The output dc power is measured by the Yokogawa WT310 power meter and the RF voltage waveforms are monitored using the LeCroy HDO4054 oscilloscope. The thermal camera is used for temperature monitoring.

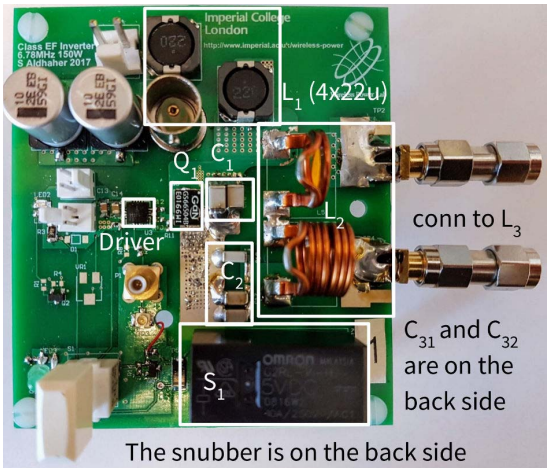

Fig. 11. Photograph of the Class EF inverter.

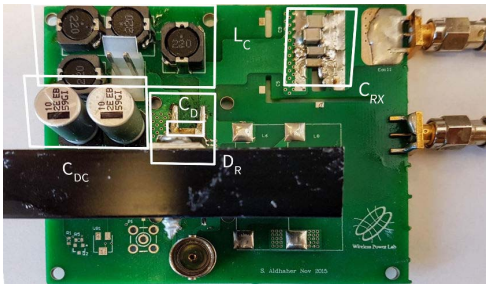

Fig. 12. Photograph of the Class-E rectifier.

TABLE I
TX AND RX COMPONENT VALUES

Inverter:	**Standalone [21]**	**Coupled**	
	Simulated	Simulated	Prototype
L_1	88 µH	88 µH	88 µH
L_2	270 nH	270 nH	283 nH
L_3	1.42 µH	1.42 µH	1.42 µH
C_1	830 pF	830 pF	660 pF
C_2	718 pF	718 pF	696 pF
C_3	480 pF	—	—
C_{3_1}	—	530 pF	526 pF
C_{3_2}	—	4.7 nF	4.7 nF
Q_1	50 mΩ (R_{on})	50 mΩ (R_{on})	GS66504B
R_S	—	10 kΩ	10 kΩ
L_S	—	250 nH	250 nH
k_{TX}	—	−0.0595	−0.0595
D	0.32	0.32	0.32
f	6.78 MHz	6.78 MHz	6.81 MHz
Rx load:	**Resistive**	**Rectifier**	
	Simulated	Simulated	Prototype
L_C	88 µH	88 µH	88 µH
L_{RX}	1.7 µH	1.7 µH	1.7 µH
C_D	—	33 pF	30 pF
C_{DC}	—	20 µF	20 µF
C_{RX}	324 pF	498 pF	498 pF
D_R	—	2 x C3D1P7060Q	C3D02060F

modules locations only, which is a strong advantage in terms of power consumption.

On top of the transmitter path, the receiver unit is able to continuously slide through the Tx path. It is also possible to transfer power to multiple receivers using different pairs of inverters, by ensuring a pair of inactive coils in between two pairs of the active ones, to avoid unwanted multiple couplings.

In the prototyped Class E rectifier, the Wolfspeed/CREE C3D02060F diode is adopted in place of the two C3D1P7060Q, due to the inaccuracy of the SPICE model of the latter in describing the diode capacitance, which causes unwanted nonzero reactance at the rectifier input. This allows a lower capacitance, of the order of 20 pF, at the expense of a 1% reduction of the peak efficiency. However, this is found to be necessary to achieve a proper working system. Both devices are based on wide bandgap semiconductors, which allow higher efficiencies, power densities, breakdown voltages, and low stray capacitances.

Table I reports all the component values of the inverters and of the receiver. Both the predicted and the actual ones used in the prototype are reported. For the Tx side, both the standalone and the coupled inverter configurations are reported. For the Rx side, two configurations are considered: 1) the purely

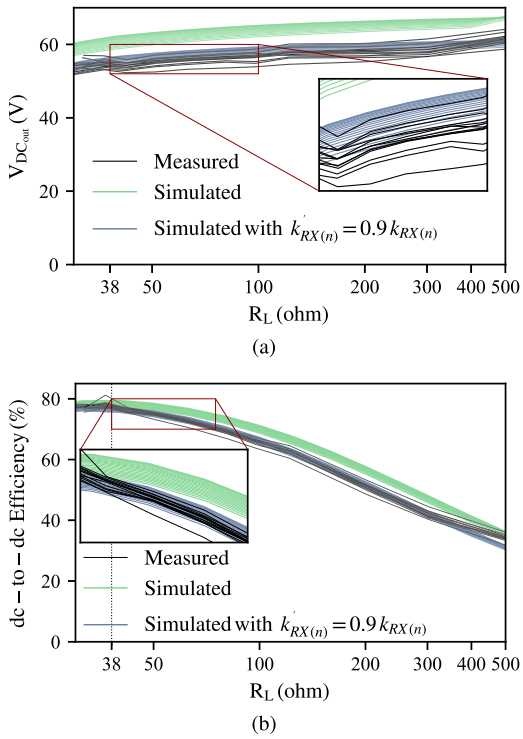

Fig. 13. (a) Measured and simulated output dc voltage and (b) system efficiency versus dc load, for 20 positions over a 60-cm Rx displacement. For 0 cm, the Rx and TX_1 axes are aligned; for 60 cm, the Rx and TX_4 axes are aligned. The curves are almost indistinguishable (for a given load, no significant variations of the system performance are experimentally verified). Insets are used to highlight the differences. The two families of simulated plots are obtained using $k_{RX(n)}$, as computed in (5), and with $k'_{RX(n)} = 0.9k_{RX(n)}$, which better matches the measured coupling.

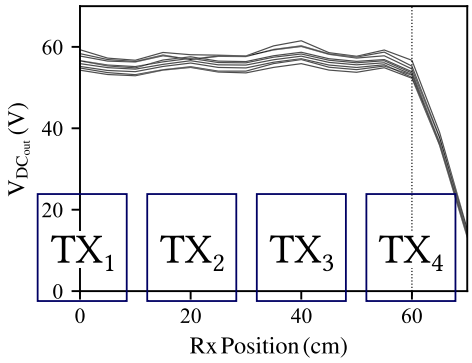

Fig. 14. $V_{dc_{out}}$ versus an extended Rx position, with the load as a parameter. Each line is a different dc load. For 0 cm, the Rx and TX_1 axes are aligned, and the couple TX_1 TX_2 is active; for 60 cm, the Rx and TX_4 axes are aligned and a further fifth coil should be activated (not available in the present prototype). Starting from this position, the output voltage immediately drops.

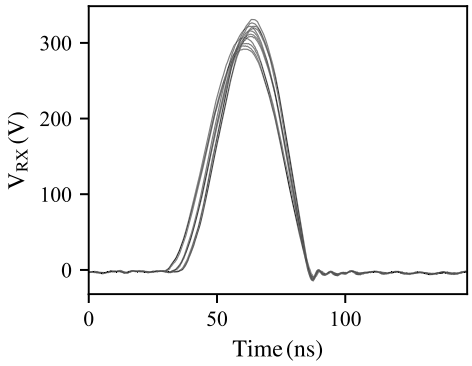

Fig. 15. Voltage on D_R (V_{RX}) measured for all the combination of four Rx positions (0, 5, 10, and 15 cm) and three loads (60, 80, and 120 Ω).

resistive variable load, in series with the $C_{RX} - L_{RX}$ resonator and 2) the rectifier. Some component values of the prototype are different from the predicted ones due to the fine tuning needed for the experimental setup. The optimum operating frequency of the prototype was found to be 6.81 MHz to achieve ZVS.

A. Entire WPT System Characterization With the Moving Rx

The receiver is moved over the entire Tx path and the dc output voltage is measured. Fig. 13(a) shows the simulated and measured dc output voltage and Fig. 13(b) shows the overall dc-to-dc efficiency. Simulation results belong to two different models of the RF-to-RF link: the first one uses the link Z-matrix computed by full-wave EM simulation; the second one uses a coupled coils model with the coupling coefficient reduced by 10% ($k'_{RX(n)} = 0.9\,k_{RX(n)}$), which better matched the VNA measurements of the RF link, corresponding to a slightly longer Tx–Rx effective distance. The model with $k'_{RX(n)}$ is in a very good agreement with the measurements. The key aspects of these experimental plots are the excellent flatness of $V_{dc_{out}}$ that the present design is able to ensure, regardless of the receiver position and load. Fig. 13(b) shows the efficiency compared again with the two simulation models. The maximum efficiency is 80% with an output power of 100 W. As previously stated, the goal of 100 W is chosen for validating the design of the entire dc-to-dc system, while ensuring safe measurement conditions. A 70-V dc bias is needed to reach this output dc power. Choosing a higher dc bias increases the maximum efficiency and allows a higher output dc power and voltage, but with no added value to the design proposed in this paper. The chosen GaN device allows the inverter to operate with voltages as high as 100 V, predicted by simulation to enable an output dc power of 160 W into a 35-Ω load, with a dc-to-dc efficiency of about 84%. The maximum dc voltage is actually not limited by the GaN and SiC devices, but by the overheating of L_2, which reaches 80 °C with a 70-V input.

Fig. 14 shows the measured dc output voltage versus an Rx path, which exceeds the design path and highlights that the flatness property is ensured only if the *virtual* series connection is guaranteed, while it is lost as soon as the receiver moves out of the design path. Fig. 15 shows the measured voltage across D_R: the peak value of 300 V is well below the 600-V breakdown voltage, and the duty-cycle is only slightly modified (less than 6%) by load changes, ensuring an almost constant dc component of the voltage across the diode, without any output current ripple.

A loss budget can finally be estimated by considering constant (for the system in idle mode) and variable (with the output power) losses. With regard to the first contribution, the

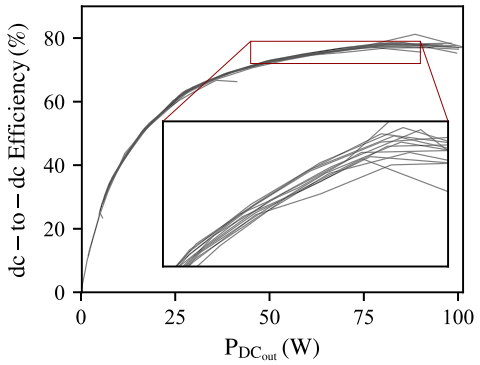

Fig. 16. DC–dc efficiency as a function of $P_{\mathrm{dc_{out}}}$. For each position (a different line), the load is swept ($30 < R_L < 500$) to obtain the resulting output power range with a 70-V $V_{\mathrm{dc_{in}}}$: this confirms that the position is not detuning the inverter.

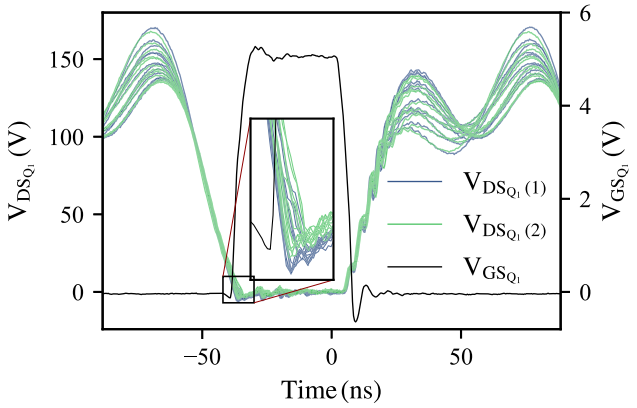

Fig. 17. GaN E-HEMT drain–source voltage of the inverters [$V_{DSQ1}(n)$, with $n = 1, 2$] measured for four Rx positions (0, 5, 10, and 15 cm) and three different loads (60, 80, and 120 Ω). The measured gate–source driving voltage waveform (V_{GSQ1} is superimposed in the same plot: the load- and position-independent soft switching operation of the inverter is experimentally verified.

measured idle power loss for both coupled inverters is 15 W. The simulated current flow in L_2, which is the components experiencing the highest temperature, is on the order of 10 A, resulting in a 3-W power loss. The power loss due to a simulated current of 7 A through L_3 is 3.5 W.

The losses variable with the output power are mainly affected by the RF chokes and are also position-dependent: when the Rx is aligned with one Tx and the output dc power is 100 W, the loss is 10 W with a 7-W contribution being from RF chokes. Hence for an output dc power of 100 W, 20 W is the total power lost in the inductors and 5 W in the other components, which confirms the advantages of using ZVS resonant converter based on wide bandgap semiconductors.

B. Coupled Inverters Characterization

Fig. 16 shows the measured dc-to-dc efficiency for a wide range of dc output powers. The lines are all well superimposed, validating experimentally the coupled inverter operation of providing the same dc output power and the same system efficiency regardless of the Rx position. From these plots, it can be observed that the dc-to-dc system efficiency exceeds 60% as the output dc power is over 20 W.

A direct measurement of the Tx output currents $I_{o(n)}$ is not feasible, since it strongly affects its operation, but it is possible to deduce that the currents through the active Tx coils are equal from Fig. 16 and from thermal measurements: if there was a change in the phases of the Tx coil currents due to a different Rx position, this would cause a significant increase of the inverter losses due to the degradation of the ZVS operation and would overheat Q_1. Indeed, a phase shift of the current $I_{o(n)}$ directly affects the inverter ability to operate in soft-switching conditions, while the ZVS is guaranteed by the plots shown in Fig. 17, where the measured drain–source voltage waveforms of the two active inverters are reported, for various combinations of dc loads and Rx positions. The soft-switching operation is ensured for both inverters and therefore the desired phase coherence of the currents $I_{o(n)}$ is expected. Furthermore, tests carried out with the thermal camera confirm that no overheating is experienced by the GaN devices. A further confirmation comes from the measured constant $V_{\mathrm{dc_{out}}}$ in Fig. 14, which proves the *virtual* series connection between the coupled inverters. Since the output voltage is related to the absolute value of V_{RX}

$$V_{\mathrm{RX}} = M_{\mathrm{TX}_1} I_{o(1)} + M_{\mathrm{TX}_2} I_{o(2)} \tag{22}$$

a phase difference would add two out-of-phase contributions and therefore a lower V_{RX} also dependent on the Rx position.

IV. Conclusion

The piecewise modeling and design of an IPT system at 6.78 MHz for *on-the-move* powering has been presented. First, the RF-to-RF link, consisting of an array of Tx coils and a moving Rx coil, is optimized. Each Tx coil is excited by a coupled load-independent Class EF Inverter, which ensures soft switching and constant output RF current, enforcing a *virtual* series connection. The receiving subsystem, based on a Class E rectifier, is designed and embedded in the entire system to provide a quasi-resistive RF load to the inverter, while having constant output voltage.

The result is an optimized and fully modular dc-to-dc WPT system, capable of operating for several different Rx loading conditions and positions, which can be lengthened or shortened according to the specific application, without any need for further design efforts. With a dc input voltage of 70 V, the dc-to-dc efficiency is 80% and the dc output power is 100 W. Only the dc feed and the control logic are distributed along the path while the RF signal is generated locally, with the twofold benefit of minimizing the RF leakage and of providing full scalability.

References

[1] W. C. Brown, "The history of power transmission by radio waves," *IEEE Trans. Microw. Theory Techn.*, vol. MTT-32, no. 9, pp. 1230–1242, Sep. 1984.

[2] H. Kim *et al.*, "Coil design and measurements of automotive magnetic resonant wireless charging system for high-efficiency and low magnetic field leakage," *IEEE Trans. Microw. Theory Techn.*, vol. 64, no. 2, pp. 383–400, Feb. 2016.

[3] M. P. Kazmierkowski and A. J. Moradewicz, "Unplugged but connected: Review of contactless energy transfer systems," *IEEE Ind. Electron. Mag.*, vol. 6, no. 4, pp. 47–55, Dec. 2012.
[4] C.-S. Wang, O. H. Stielau, and G. A. Covic, "Design considerations for a contactless electric vehicle battery charger," *IEEE Trans. Ind. Electron.*, vol. 52, no. 5, pp. 1308–1314, Oct. 2005.
[5] C.-S. Wang, G. A. Covic, and O. H. Stielau, "Power transfer capability and bifurcation phenomena of loosely coupled inductive power transfer systems," *IEEE Trans. Ind. Electron.*, vol. 51, no. 1, pp. 148–157, Feb. 2004.
[6] T. Fujita, T. Yasuda, and H. Akagi, "A dynamic wireless power transfer system applicable to a stationary system," *IEEE Trans. Ind. Appl.*, vol. 53, no. 4, pp. 3748–3757, Jul./Aug. 2017.
[7] R. Trevisan and A. Costanzo, "A 1-kW contactless energy transfer system based on a rotary transformer for sealing rollers," *IEEE Trans. Ind. Electron.*, vol. 61, no. 11, pp. 6337–6345, Nov. 2014.
[8] R. Trevisan and A. Costanzo, "A UHF near-field link for passive sensing in industrial wireless power transfer systems," *IEEE Trans. Microw. Theory Techn.*, vol. 64, no. 5, pp. 1634–1643, May 2016.
[9] F. Mastri, A. Costanzo, and M. Mongiardo, "Coupling-independent wireless power transfer," *IEEE Microw. Wireless Compon. Lett.*, vol. 26, no. 3, pp. 222–224, Mar. 2016.
[10] J. Shin *et al.*, "Design and implementation of shaped magnetic-resonance-based wireless power transfer system for roadway-powered moving electric vehicles," *IEEE Trans. Ind. Electron.*, vol. 61, no. 3, pp. 1179–1192, Mar. 2014.
[11] T. Ohira, "The kQ product as viewed by an analog circuit engineer," *IEEE Circuits Syst. Mag.*, vol. 17, no. 1, pp. 27–32, 1st Quart., 2017.
[12] J. P. C. Smeets, T. T. Overboom, J. W. Jansen, and E. A. Lomonova, "Comparison of position-independent contactless energy transfer systems," *IEEE Trans. Power Electron.*, vol. 28, no. 4, pp. 2059–2067, Apr. 2013.
[13] J. P. C. Smeets, T. T. Overboom, J. W. Jansen, and E. A. Lomonova, "Modeling framework for contactless energy transfer systems for linear actuators," *IEEE Trans. Ind. Electron.*, vol. 60, no. 1, pp. 391–399, Jan. 2013.
[14] F. Lu, H. Zhang, H. Hofmann, and C. C. Mi, "A dynamic charging system with reduced output power pulsation for electric vehicles," *IEEE Trans. Ind. Electron.*, vol. 63, no. 10, pp. 6580–6590, Oct. 2016.
[15] A. Pacini, F. Mastri, R. Trevisan, D. Masotti, and A. Costanzo, "Geometry optimization of sliding inductive links for position-independent wireless power transfer," in *IEEE MTT-S Int. Microw. Symp. Dig.*, May 2016, pp. 1–4.
[16] A. Pacini, F. Mastri, R. Trevisan, D. Masotti, and A. Costanzo, "Theoretical and experimental characterization of moving wireless power transfer systems," in *Proc. Eur. Conf. Antennas Propag. (EuCAP)*, Apr. 2016, pp. 1–4.
[17] Z. Zhang and K. T. Chau, "Homogeneous wireless power transfer for move-and-charge," *IEEE Trans. Power Electron.*, vol. 30, no. 11, pp. 6213–6220, Nov. 2015.
[18] M. Chabalko, J. Besnoff, M. Laifenfeld, and D. S. Ricketts, "Resonantly coupled wireless power transfer for non-stationary loads with application in automotive environments," *IEEE Trans. Ind. Electron.*, vol. 64, no. 1, pp. 91–103, Jan. 2017.
[19] A. Pacini, S. Aldhaher, A. Costanzo, and P. D. Mitcheson, "Design of a position-independent end-to-end inductive WPT link for industrial dynamic systems," in *IEEE MTT-S Int. Microw. Symp. Dig.*, Jun. 2017, pp. 1053–1056.
[20] *CST Microwave Studio 2013*. Accessed: Sep. 2017. [Online]. Available: http://www.cst.com
[21] S. Aldhaher, P. D. Mitcheson, and D. C. Yates, "Load-independent class EF inverters for inductive wireless power transfer," in *Proc. IEEE Wireless Power Transf. Conf. (WPTC)*, May 2016, pp. 1–4.
[22] M. K. Kazimierczuk and D. Czarkowski, *Resonant Power Converters*, 2nd ed. Hoboken, NJ, USA: Wiley, 2012.
[23] M. K. Kazimierczuk, "Analysis of class E zero-voltage-switching rectifier," *IEEE Trans. Circuits Syst.*, vol. 37, no. 6, pp. 747–755, Jun. 1990.
[24] J. J. Jozwik and M. K. Kazimierczuk, "Analysis and design of class-E_2 DC/DC converter," *IEEE Trans. Ind. Electron.*, vol. 37, no. 2, pp. 173–183, Apr. 1990.
[25] J. A. Santiago-González, K. M. Elbaggari, K. K. Afridi, and D. J. Perreault, "Design of class E resonant rectifiers and diode evaluation for VHF power conversion," *IEEE Trans. Power Electron.*, vol. 30, no. 9, pp. 4960–4972, Sep. 2015.

Alex Pacini (GS'12) received the master's degree *(summa cum laude)* in electrical and telecommunication engineering from the University of Bologna, Bologna, Italy, in 2015, where he is currently pursuing the Ph.D. degree.

His current research interests include antenna systems, near-field wireless power transfer, resonant converters, and RF/microwave circuit and systems design.

Alessandra Costanzo (A'99–M'02–SM'13) is currently an Associate Professor with the University of Bologna, Bologna, Italy. She is involved in research activities dedicated to the wireless power transmission, adopting both far-field and near-field solutions, for several power levels and operating frequencies. She has authored over 200 scientific publications on peer-reviewed international journals and conferences and several chapter books.

Dr. Costanzo is a co-founder of the EU COST Action IC1301 WiPE Wireless Power Transfer for Sustainable Electronics, where she chairs WG1: Far-Field Wireless Power Transfer. She is the Chair of the MTT-26 Committee on Wireless Energy Transfer and Conversion and a member of the MTT-24 Committee on RFID. Since 2016, she has been the Steering Committee Chair of the new IEEE JOURNAL OF RADIO FREQUENCY IDENTIFICATION. She is an IEEE MTT Society (MTT-S) representative and a Distinguished Lecturer of the Council on Radio Frequency Identification, where she also serves as an MTT-S Representative. She serves as an Associate Editor for the IEEE TRANSACTIONS ON MICROWAVE THEORY AND TECHNIQUES, the *Cambridge International Journal of Microwave and Wireless Technologies*, and the *Cambridge International Journal of Wireless Power Transfer*.

Samer Aldhaher received the B.Sc. degree in electrical engineering from the University of Jordan, Amman, Jordan, in 2010, and the Ph.D. degree (with a focus on the design and optimization of switched-mode circuits and development of novel electronic tuning methods for inductive power transfer applications) from Cranfield University, Bedford, U.K., in 2014.

He is currently a Research Associate with the Control and Power Group, Department of Electrical and Electronic Engineering, Imperial College London, London, U.K. His current research interests include the design of multimegahertz dc/ac inverters and rectifiers, and wireless power transfer applications based on resonant inductive links.

Paul D. Mitcheson (SM'12) received the M.Eng. degree in electrical and electronic engineering and Ph.D. degree in micropower motion-based energy harvesting for wireless sensor networks from Imperial College London, London, U.K., in 2001 and 2005, respectively.

He is currently a Professor of electrical energy conversion with the Control and Power Research Group, Electrical and Electronic Engineering Department, Imperial College London. His current research interests include energy harvesting, power electronics, and wireless power transfer to provide power to applications in circumstances where batteries and cables are not suitable. His research has been supported by the European Commission, the Engineering and Physical Sciences Research Council, and several companies.

Dr. Mitcheson is a Fellow of the Higher Education Academy. He is on the Executive Committee of the U.K. Power Electronics Centre.